Experimental Mechanics (2022) 62:1067–1077
https://doi.org/10.1007/s11340-022-00853-7

RESEARCH PAPER

The Role of Buckling Instabilities in the Global and Local Mechanical Response in Porous Collagen Scaffolds

B. Kim[1] · J. M. Middendorf[1] · N. Diamantides[2] · C. Dugopolski[3] · S. Kennedy[3] · E. Blahut[3] · I. Cohen[4] · N. Bouklas[1] · L. J. Bonassar[1,2]

Received: 23 July 2021 / Accepted: 11 April 2022 / Published online: 3 June 2022

Abstract

Background Porous polymer scaffolds are commonly used for regenerative medicine and tissue-engineered therapies in the repair and regeneration of structural tissues which require sufficient mechanical integrity to resist loading prior to tissue ingrowth.

Objective Investigate the connection between scaffold architecture and mechanical response of collagen scaffolds used in human tissue-engineered cartilage.

Methods We performed multi-scale mechanical analysis on two types of porous collagen scaffolds with honeycomb and sponge architectures. Confined compression testing was used to assess global non-linear mechanical response of scaffolds. Additionally, we performed confocal strain mapping combined with digital image correlation (DIC) to visualize local mechanical instabilities and compared local strain distributions between scaffold architectures.

Results The global response of both scaffold architectures followed a pattern characteristic of cellular solids, with a linear region, a plateau region, and a densification region. Macro-scale non-linear responses corresponded to local-scale instabilities such as snap-through buckling. On the local-scale, a construct's compressive response depended heavily on the architecture type. Scaffolds with honeycomb architecture experienced a unimodal strain distribution throughout the scaffold depth. In contrast, scaffolds with sponge architecture tended to collapse at the boundaries.

Conclusions We demonstrated that differences in mechanical response between scaffold architectures were detected primarily at the micro-scale which stems from the disparity in pore architecture. As such, tools like confocal strain mapping combined with DIC are critical for designing and optimizing architectures for porous materials. Observing local instabilities in porous materials is important not only for tuning mechanical response, but also for controlling mechanical events that influence cellular and tissue behavior.

Keywords Soft Porous Materials · Digital Image Correlation · Compression · Tissue Engineering

Introduction

Tissue engineering techniques often utilize three-dimensional porous collagen scaffolds as a template for cell attachment and extra cellular matrix synthesis [1, 2]. The architecture of collagen scaffolds in tissue engineering techniques has a significant impact on cell attachment and proliferation [3, 4]. Clinical studies have shown that tissue-engineered cartilage constructs have successfully integrated with the surrounding native tissue and filled in focal defects while maintaining cell viability [5]. Furthermore, several tissue-engineered cartilage products including MACI® [6] and NeoCart™ [7] use porous collagen scaffolds and are either approved by the FDA or are currently undergoing clinical trials. During the early stage of engineered cartilage implantation, porous collagen scaffolds provide necessary mechanical support and dictate the local mechanical environment for the cells. These scaffolds will be subject to the same *in vivo* loads of native articular cartilage, up to 40% strain and contact pressure of 12.54 MPa [8–10]. Indeed, previous work has

✉ L. J. Bonassar
lb244@cornell.edu

[1] Sibley School of Mechanical and Aerospace Engineering, Cornell University, Ithaca, NY, USA

[2] Meinig School of Biomedical Engineering, Cornell University, Ithaca, NY, USA

[3] Histogenics Corporation, Waltham, MA, USA

[4] Department of Physics, Cornell University, Ithaca, NY, USA

shown that porous scaffolds without any new matrix deposition can buckle at sub-physiological strains [11, 12]. These local instabilities (e.g., buckling) within collagen scaffolds compromise overall performance [13] and produce strain gradients that may inhibit tissue integration due to the large strain gradient. Additionally, these large deformations could be detrimental for the survivability of chondrocytes, as they produce high compressive strain that increases the probability of cell death [14]. Therefore, understanding the buckling mechanics of porous collagen scaffolds is crucial for optimizing the *in vivo* function and success of tissue-engineered cartilage constructs directly following the implantation.

Existing frameworks for understanding the mechanics of porous structure effectively describe the behavior of porous materials like aluminum foam and wood. Such frameworks have been extended to brittle biological tissues such as bone, and numerous studies have found similar compressive mechanical responses among trabecular bone, aluminum foam, and wood [15]. Despite the difference in composition and base materials of these porous cellular solids, all compressive mechanical responses arise from local instabilities at the pore level. Furthermore, variation in pore size distribution and shape leads to different deformation patterns in porous structures [16]. Additionally, these studies have provided a theoretical basis to explain the typical stress–strain curves observed experimentally. Such curves typically contain three regions: a linear region, a plateau region, and a densification region. The plateau region is from the emergence of instabilities within the structure, and the densification region is from the pores of the structure collapsing on top of each other. These phenomena have been well studied at the macro-scale, but the connection between the non-linear behavior of stress–strain and local instabilities have never been directly observed. In particular, much less is known about the connection between macro-scale and micro-scale behavior of soft, viscoelastic porous materials like collagen scaffolds typically used in tissue engineering applications. Notably, collagen scaffolds have a wide variety of pore size distributions and architecture [17–19]. Pore architecture of the scaffolds is generally designed to optimize biological considerations such as cell proliferation and nutrient transfer with little attention to its effects on scaffold mechanics [3, 20]. As such, the relationship between pore architecture and mechanical performance of collagen scaffolds is poorly understood.

The compressive behavior of collagen scaffolds can be better understood by investigating local strain fields that occur during loading. Over the past decade, we have developed techniques for the visualization of local strain fields for collagen based soft tissue-engineered constructs [13, 21–24]. These techniques use fast confocal microscopy combined with digital image correlation (DIC) to measure strain fields with a spatial resolution of 41.4 μm. More recently, we have applied these techniques to measure the mechanics of tissue-engineered cartilage at various stages of maturity [13]. These studies demonstrate that the emergence of instabilities is a critical feature of the mechanics of these constructs at the early stage of development. However, the effect of pore architecture on local strain fields and instabilities is not known.

With this in mind, the objective of this study was to identify how pore architecture affects global and local compressive behavior of collagen scaffolds for tissue engineering. We investigated commercially available collagen scaffolds made of freeze-dried type 1 collagen with two types of architecture: honeycomb-like (monodisperse pores) and sponge-like (polydisperse pores). To investigate the relationship between scaffold architecture and compressive mechanics, the current study identified transitions in the global stress–strain curve under compression and related these transitions to emerging instabilities and local strain field as measured by confocal strain mapping.

Materials and Methods

Collagen Scaffolds Preparation

Two different architectures of collagen scaffolds were tested: honeycomb collagen scaffolds manufactured by Histogenics Corp. (Waltham, MA) provided by courtesy of Stephen Kennedy, and sponge collagen scaffolds manufactured by Koken CO., LTD (Tokyo, Japan), (CSH -96). Both Histogenics and Koken collagen scaffolds were made from type I bovine dermis collagen and had pore sizes ranging from 100 – 200 μm in diameter, according to the manufacturing specification. Therefore, any mechanical behavior differences observed between the two types of scaffolds could be solely based on the architecture. Collagen scaffolds were cut using 2 mm and 6 mm biopsy punches (Integra York PA, Inc., York, PA) with pores aligned in the axial direction (Fig. 1(A), z-axis).

Global Mechanical Properties Identification

Collagen scaffolds were tested in confined compression (n = 12) to identify global mechanical properties. Scaffolds with 2 mm diameter and 1.5 mm height cylinders were placed in a 2 mm diameter confining chamber [25]. Then, samples were submerged in phosphate-buffered saline (PBS, Corning, Manassas, VA) and covered with a porous platent. The confining chamber and sample were then mounted on a Bose EnduraTEC ELF 3200 (Eden Prairie, MN). The collagen scaffolds were then compressed to 50% of their original height using a triangular wave displacement control at 0.1 mm/s to maintain a quasi-static condition. We tested the

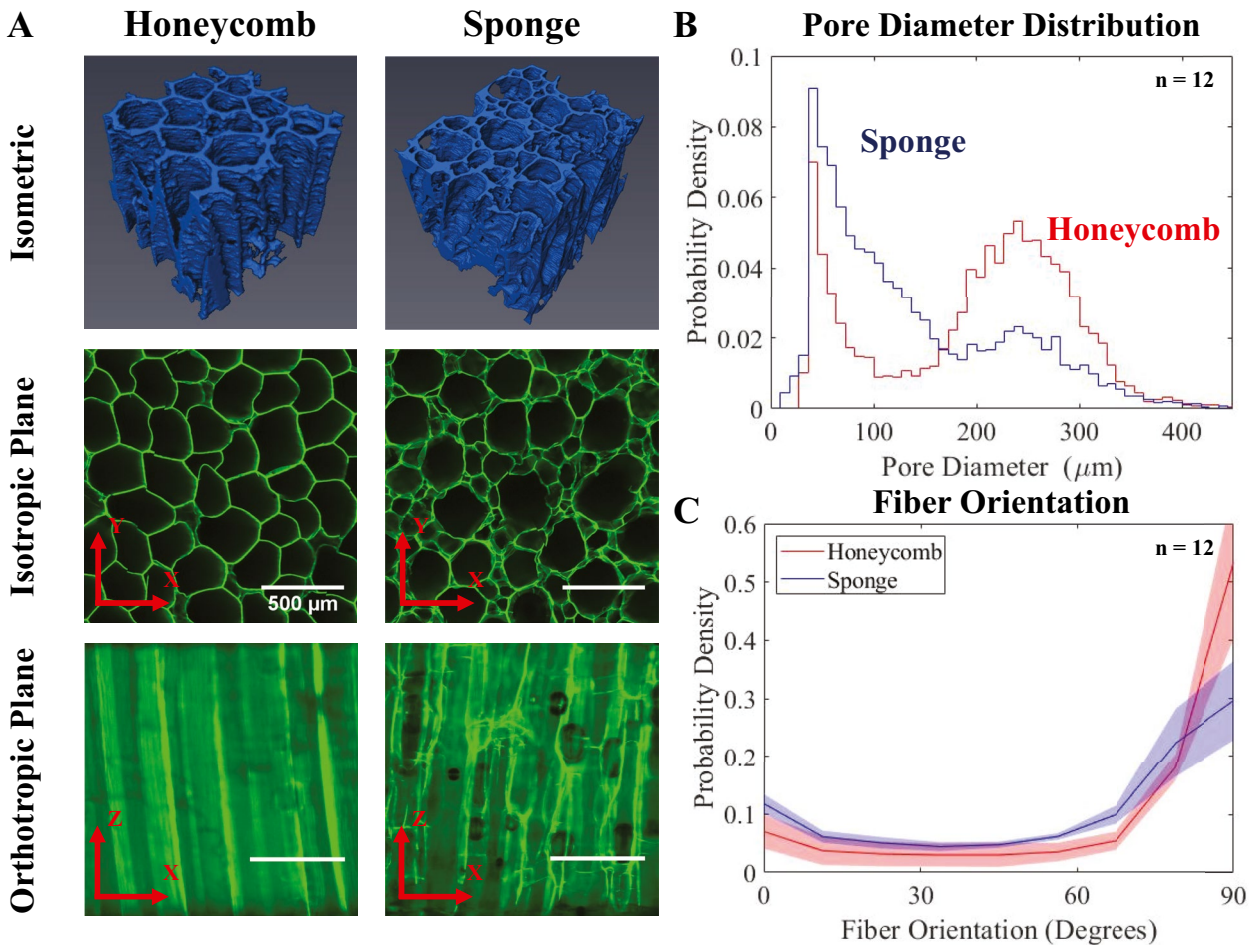

Fig. 1 Honeycomb and sponge collagen scaffolds showed difference in architecture **A**) Reconstructed models from µCT images and confocal microscope images **B**) Pore diameter distribution of the scaffolds **C**) Fiber orientation of the scaffolds with shaded region representing standard deviation

compressive response of the orthotropic plane (Fig. 1(A), z axis) of the collagen scaffolds due to clinical relevancy, as the orthotropic plane carries most of the compressive load once tissue-engineered constructs are implanted into patients [5, 7]. In addition, confined compression was used to mimic the *in vivo* loading condition of the collagen scaffolds. Once the collagen scaffolds are implanted, they are surrounded by stiffer native tissue creating confined compression condition. A stress–strain curve was obtained for each collagen scaffold by normalizing compressive load to the original cross-sectional area and sample height.

Global parameters such as buckling stress and strain were calculated using the stress–strain curves [24]. Briefly, we fitted a linear regression to both the linear and plateau regions, and the intersection between the two regression lines was defined as the buckling point. Corresponding stress and strain from the buckling point were defined as the buckling stress and buckling strain. Similarly, we fitted a linear regression to the plateau and collapse region, and the intersection between the two regression lines was defined as the densification point. We defined collapse as the deviation from the linear region of the stress–strain curve.

Local Compressive Strain Mapping and Analysis

The local compressive response of the scaffolds were acquired based on an established protocol [13, 21–23, 26]. The cylindrical scaffolds were bisected into hemi-cylinders and stained with 14 µg/mL 5-dichlorotriazinyl-aminofluorescein (5-DTAF, Molecular Probes, Grand Island, NY) for 30 minutes. Stained scaffolds were then washed in PBS for 20 minutes and mounted between two parallel plates of a Tissue Deformation Imaging Stage. The scaffolds were then placed on an inverted Zeiss LSM 510 5 live confocal microscope with a Zeiss 5×objective and imaged using a 488 nm laser (Carl Zeiss AG, Oberkochen, Germany). Initially, the mounted scaffolds were compressed to 1.5 mm to remove the swelling. A triangular displacement function with an amplitude of 750 µm was

applied to one of the parallel plates at 0.1 mm/s. During compression, load and video were recorded. The compressive load was measured at a sampling rate of 1000 Hz, and the video was recorded with the frame rate of 20 frames per second.

The local Lagrange strain was obtained using an open-source MATLAB-based Digital Image Correlation (DIC) program, NCORR [26]. Local deformation from compression videos was tracked with a subset spacing of 41.4 μm and a subset radius of 82.9 μm.

Collagen Scaffold Characterization

The isotropic plane (Fig. 1(A), x–y plane) of each stained scaffold was imaged using an inverted confocal microscope. Using ImageJ, images were binarized and the 'Analyze Particles' function was applied to calculate the area of each pore. The radii of the pores were calculated under the assumption that the pores were perfect circles. A cross-sectional plane (Fig. 1(A), x-z plane) was also captured to visually identify the characteristics of each type of collagen scaffold. Cross-sectional images of all samples were analyzed by ImageJ using the 'Directionality' function to characterize fiber orientation.

Local Strain Distribution Analyses

Confined compression testing can capture the *in vivo* condition of the collagen scaffolds, but the mechanical response of the sample cannot be visually captured due to the presence of the confining chamber. To understand the role of local instabilities in the global behavior of each type of scaffold, we applied the confocal strain mapping method described above to investigate the linear region, buckling region, plateau region, and densification region. Specifically, we used the transitions between linear to plateau, and plateau to densification regions to inform the local strain distribution. Based on the local compressive strain analysis, we chose to analyze the local strain distribution at 15% and 30% bulk strain, as collapse bands started to form at 15%, and local densification occurred at 30% bulk strain. This method enabled the identification of local instabilities as manifest in local regions of high strain (e.g., 2 times of bulk strain).

To understand how pore structure controls the evolution of instabilities in these scaffolds, we examined the statistical distribution of local strain at various levels of compression. Samples with wide and bimodal local strain distribution would contain localized region of instabilities. In contrast, samples with plateau distribution would be an indication for unimodal strain distribution across the structures. To achieve this, each local deformation subset was normalized using the bulk compression value of each sample, and the normalized subset strain values were plotted as a histogram with bin width of 0.1 normalized strain. The distribution trend of the histogram was acquired using the Kernel smoothing function fit method. For depth-dependent strain distribution analysis, normalized compressive strain matrix of each sample was averaged row wise.

Statistical Analysis

Two-sample hypothesis testing (t-tests) was used to determine the statistical significance of global properties of the two types of collagen scaffolds. The difference in global mechanical properties was considered significant at $p < 0.05$. Post hoc power (β) of the statistical test was calculated for each global mechanical property by comparing mean value and standard deviation of honeycomb global parameter to the mean value of sponge global parameter. The significance level of the test was set to 0.05.

Local compressive strain values of sponge and collagen scaffolds were plotted as a histogram at 15% and 30% bulk strain with 0.1 bin size. The trend of each histogram was fitted with a trendline using a kernel distribution. The trendlines were then compared using Kolmogorov–Smirnov method for statistical significance.

Results

Collagen Scaffold Architectures and Global Mechanical Properties

We first identified the architectural differences between honeycomb and sponge collagen scaffolds. Microscopic images revealed that there were differences in both pore size distribution and fiber orientation for the honeycomb and sponge scaffolds (Fig. 1). While both collagen scaffolds had bimodal distributions in pore size, honeycomb collagen scaffolds had distinct peaks at approximately 250 μm and 50 μm (Fig. 1(B), Online Resource 1 and 2). In sponge scaffolds, pores were more widely distributed but with similar sizes. Vertical cross-sectional images showed that honeycomb scaffolds consisted of tubular pores with mostly solid walls. On the other hand, sponge scaffolds had a hierarchical structure where the larger tubular pores were surrounded by walls containing smaller spherical pores. These structural differences were also characterized by the fiber orientation in the cross section (Fig. 1(C)). Honeycomb scaffolds had a higher degree of fiber alignment in the vertical direction (z-axis), while sponge scaffolds had a more distributed fiber orientation across the angles. This further confirmed that sponge scaffolds had more highly connected inner architecture while honeycomb scaffolds had mostly axially oriented tubular pores throughout the scaffold.

Global parameters of both types of collagen scaffolds were obtained through confined compression testing (Fig. 2(A)). Averaged stress–strain curves for both sponge

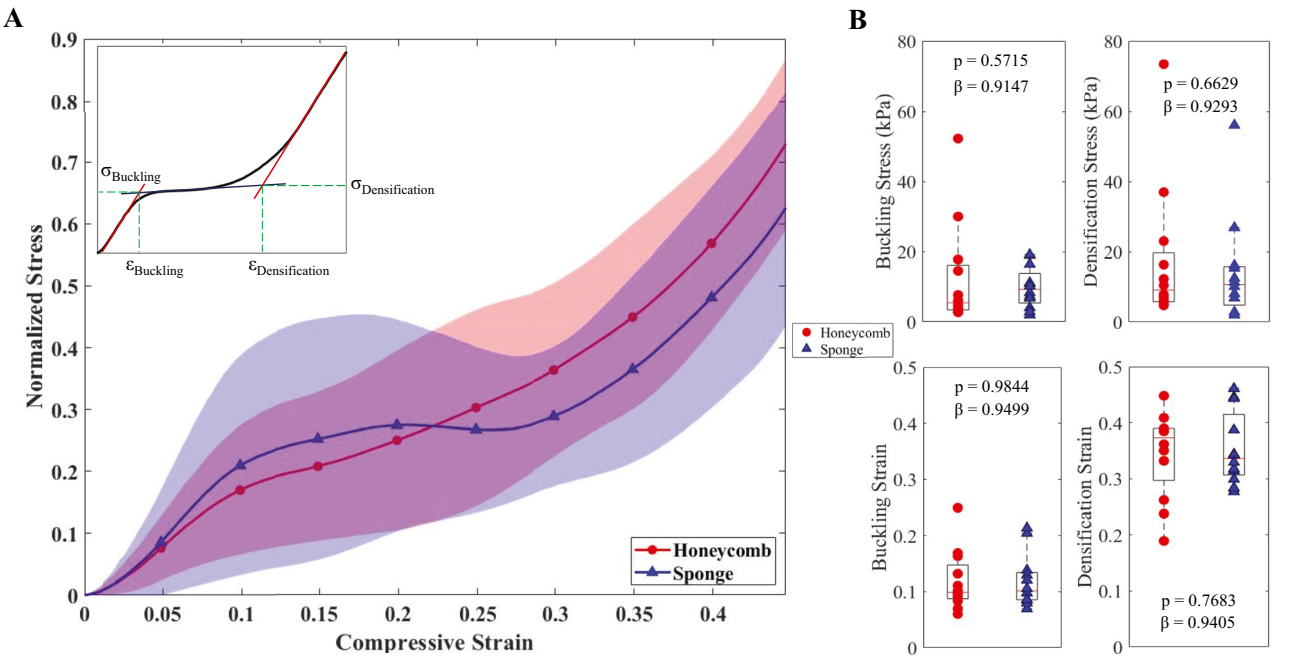

Fig. 2 Global parameters showed no statistical significance between the two types of scaffolds **A**) Averaged stress–strain curve from the global collagen scaffold compression testing with shaded region representing standard deviation **B**) No difference in global parameters between honeycomb and sponge scaffolds (n = 12)

and honeycomb scaffolds showed similar behavior. We found that both scaffolds displayed plateau behavior in their stress–strain curves approximately at 5% global strain and densified at 30% global strain with no significant difference in any of the measured global parameters (for honeycomb and sponge scaffolds respectively, average buckling stress: 12.50 kPa, 9.83 kPa, average buckling strain: 0.12 and 0.12, average densification stress: 17.36 kPa, 14.17 kPa average densification strain: 0.34 and 0.35, $p > 0.5715$, $\beta > 0.9157$, Fig. 2(B)). Notably, there was high degree of variability in all global parameters. For example, buckling stress and buckling strain of honeycomb scaffolds had 44.72 and 119.65 coefficient of variability respectively. For sponge scaffold, they were 39.22 and 59.60 respectively. Such high variability indicated that these parameters did not fully capture the collapse behaviors.

Compressive Behaviors

To understand the source of variability in global compressive behavior, we examined individual stress–strain curves, as these curves demonstrated unstable responses (Fig. 3).

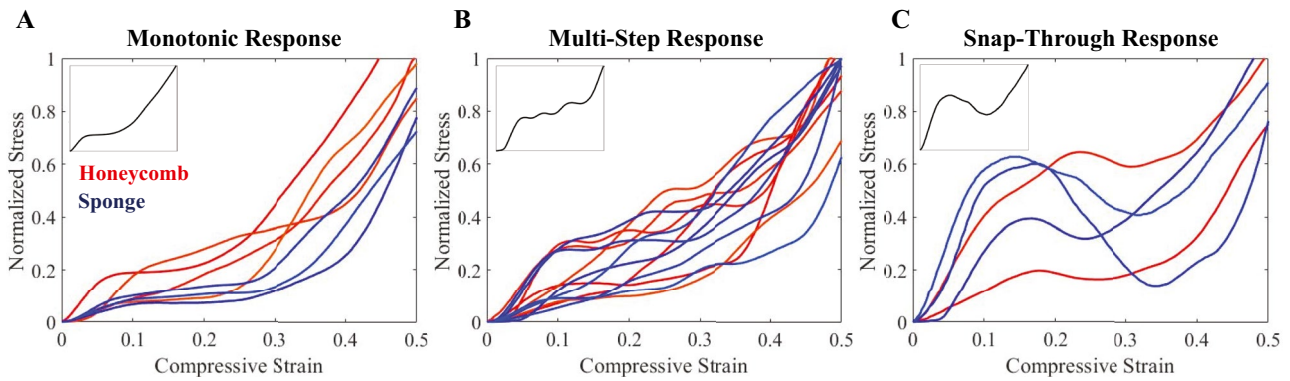

Fig. 3 Various compressive responses of porous collagen scaffolds **A**) Monotonic response from collagen scaffold compression testing **B**) Multi-Step response **C**) Snap-through buckling response

The mechanical behavior of the scaffolds was categorized into 3 different types of compressive responses noted in previous work on porous materials [15, 24]. Initially, all scaffolds displayed a toe-region, most likely due to the initial interruption of fibers at the surface of the scaffolds. After the initial non-linearity, scaffolds displayed a linear region, a plateau region, and finally a densification region (Fig. 3(A)). 4 out of 12 honeycomb scaffolds and 3 out of 12 sponge scaffolds displayed a monotonic response characterized by a smooth plateau region. Most scaffolds in both groups displayed a non-linear response characterized by a plateau region with negative slopes. Such non-linear response was concentrated in the plateau region for both types of scaffolds. We observed two types of non-linear collapsing behaviors obtained from the stress–strain curves: multi-step response and snap-through response (Fig. 3(B), (C)). During the experiment, 6 of 12 honeycomb scaffolds and 6 of 12 sponge scaffolds displayed multiple plateaus, while 2 of 12 honeycomb scaffolds and 3 of 12 sponge scaffolds displayed unstable collapsing behavior. The unstable collapsing behavior was indicated by a significant drop in stress with increasing strain, consistent with snap-through buckling. These data collectively suggest that the majority of scaffolds had compressive behavior that was dominated by instabilities.

Local Strain Mapping and Distribution Analysis

To understand the micro-scale origin of the unstable compressive behavior, we used confocal strain mapping. We visually identified unstable local responses indicated during the confined compression tests and matched them with the local stress–strain response (Fig. 4). In honeycomb scaffolds, multiple-plateaus in stress–strain curves were related to the formation of collapse bands in separate regions throughout the construct. Before the compression, the honeycomb scaffold had undeformed columnar pores along its z axis (Fig. 4(A)). At 5% bulk strain, columnar pores within honeycomb scaffolds started to buckle (Fig. 4(B)) as represented by the plateau on the stress–strain curve. At 7.5% strain, local collapse band formed in different regions within the construct (Fig. 4(C)). As bulk strain reached 10%, the local collapse bands started to propagate across the scaffolds and formed a global collapse band which led to the densification of the collapsed regions (Fig. 4(D)). Samples containing a region of decreasing stress with increasing strain were observed to exhibit unstable collapsing behavior, visually identified to be a snap-through instability (Online Resource 3).

To visualize the local Lagrangian strain field, digital image correlation analysis was conducted on the compression video taken using the confocal strain mapping

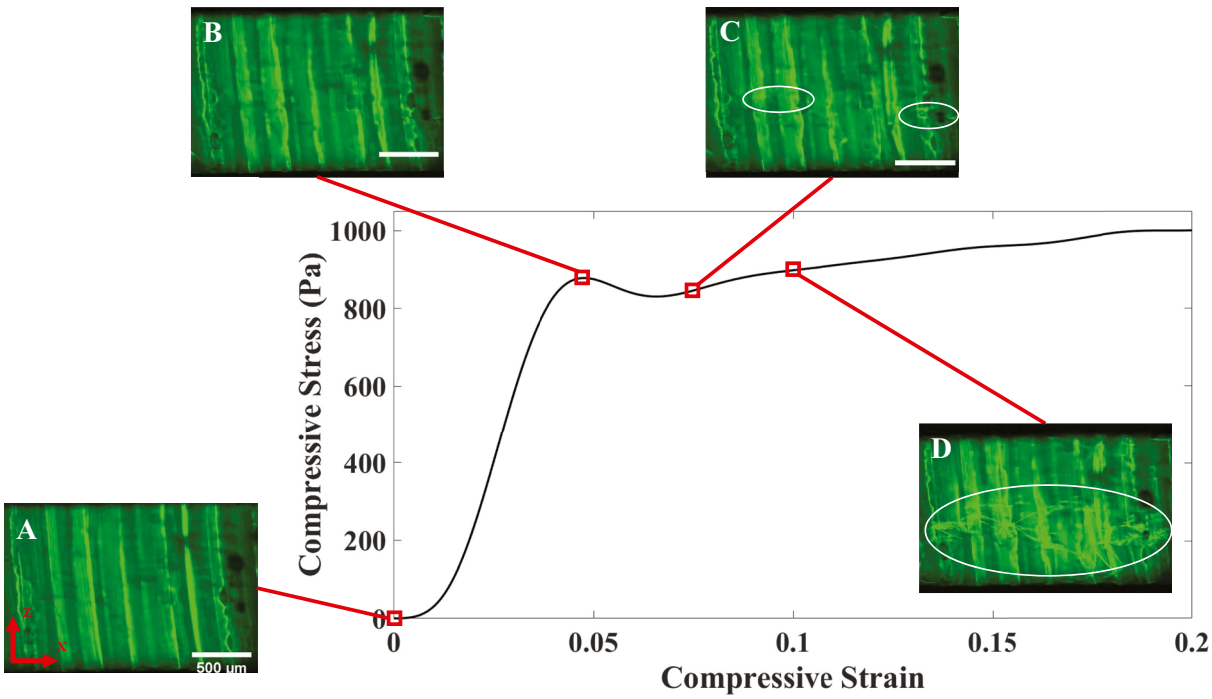

Fig. 4 Macro-scale stress–strain curves can be related to the micro-scale phenomena **A**) Undeformed honeycomb scaffold's columnar pores before the compression **B**) At the end of the linear region, slight buckling of the columnar pores was observed **C**) Deformation of the buckled regions intensified, and local collapse bands started to form **D**) Local collapse bands propagated and formed a global collapse band and local densification of the scaffolds was observed

technique. Local Lagrangian strain distribution analysis showed differences in compressive behavior of honeycomb and sponge scaffolds. High local strain within the region of interest represents concentrated deformation, likely due to the formation of local and global collapse bands. At both low (15%, Fig. 5(A)) and high strains (30%, Fig. 5(B)), honeycomb scaffolds formed collapse bands, and local strain propagated among collapse bands until it spread through the specimen. In contrast, sponge scaffolds always collapsed at the boundaries of the constructs, and the deformation was localized at the collapsed site. Non-linear behaviors at the collapsed sites indicated by the stress–strain curves could not be visualized due to the densification of the pores. Such densification caused the fibers to escape the focal plane which resulted in loss of information during the DIC analysis (Fig. 5(A) and (B)).

Local strains from all subsets within the region of interest was binned and normalized to understand the distribution of strains during compression. In each distribution, local strain was normalized to absolute global strain. Bins from 0 to -1 deformed less than the imposed global strain, while bins from -1 to -3 indicated that local regions deformed more than the global strain. At 15% global strain, local strain was concentrated below the average strain for both honeycomb and sponge scaffolds (Fig. 6(A)). Sponge scaffold had higher probability density of local strain being lower than the average strain meaning that the deformation was concentrated in one region, and rest of the construct was relatively undeformed. As bulk compressive strain increased, the local strain field of honeycomb scaffolds became more unimodally distributed. The strain distribution flattened at 30% global compressive strain (Fig. 6(B)). On the contrary, sponge scaffolds' local strain distribution became bimodal, consistent with the formation of collapse bands which concentrate high strains locally while leaving most of the local regions within the sample undeformed.

Differences in depth-dependent strain patterns between honeycomb and sponge were also observed. To quantify the differences, all local strain values were normalized to absolute global strain of each sample. The local strain values from different samples were averaged horizontally (x-axis). For sponge scaffolds, local strain was concentrated on the top or the bottom of the construct at both low and high strains. Meanwhile, honeycomb scaffolds strain was relatively unimodal throughout the construct depth (Fig. 6(C), (D)).

Discussion

The goal of this study was to investigate how collagen scaffold architecture affects global and local compressive behavior. We used two different types of commercially available collagen scaffolds, honeycomb and sponge, that had different pore-size distributions and wall architectures. During confined compression, both types of scaffolds had similar global mechanical responses as reflected in their stress–strain curves. The plateau region was dominated by instabilities at the local level that were visualized and quantified by confocal strain mapping. This analytical technique identified a stark difference in deformation patterns and local strain distributions between honeycomb and sponge scaffolds, with sponge scaffolds having more highly localized deformation as manifested in a greater frequency of high local strains.

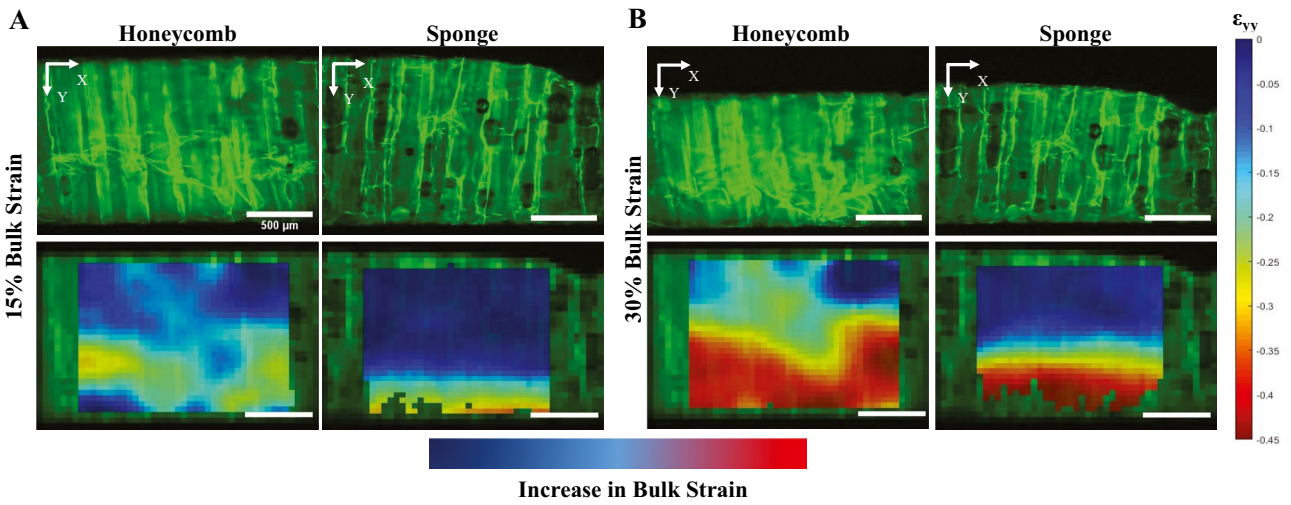

Fig. 5 Difference in local strain distribution **A**) Honeycomb scaffolds formed a collapse band across the construct while sponge scaffolds did not display any visible collapse bands **B**) Honeycomb scaffolds' local strains were distributed across the construct while sponge scaffolds' local strains continued to be concentrated at the boundary

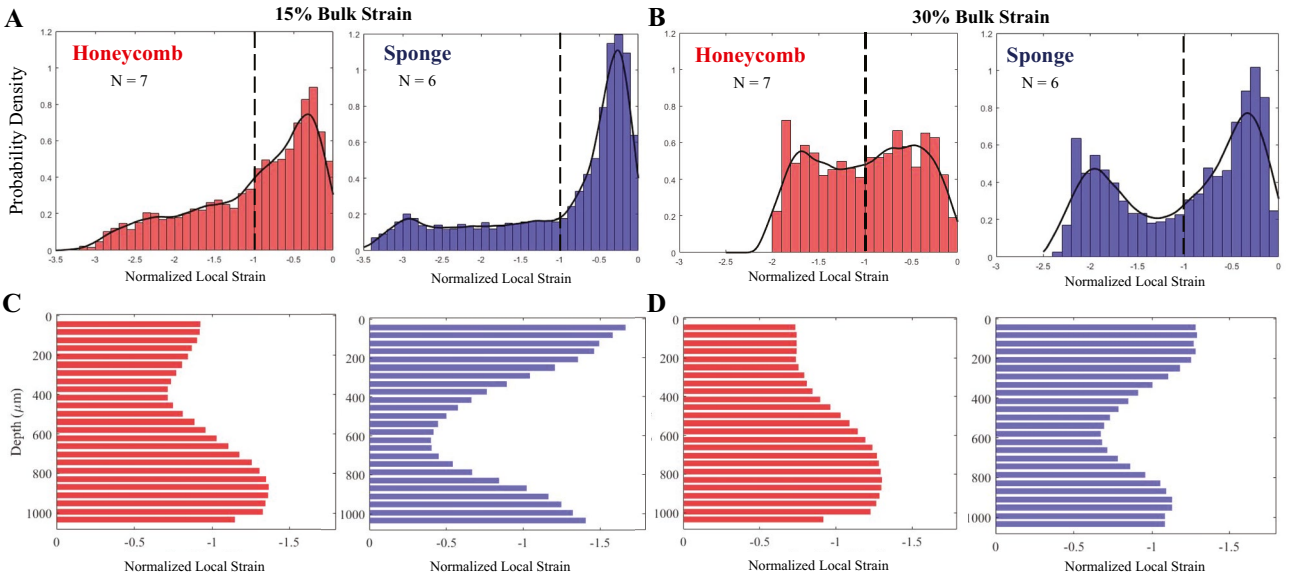

Fig. 6 Histogram of the local strain distribution **A**) Honeycomb scaffolds had a gradual decline in probability below the bulk strain, while sponge scaffolds started to show a bimodal distribution **B**) Honeycomb scaffolds had a unimodal local strain distribution while sponge scaffolds had a clear bimodal distribution **C**) Depth-Dependent (z-axis) normalized strain distribution at 15% bulk strain and **D**) at 30% bulk strain

Honeycomb scaffolds first formed one or more clearly visible collapse bands near the center of the construct, and sponge scaffolds always collapsed at the boundaries (Online Resource 4). This data collectively suggests that the pore architecture of scaffolds is directly linked to the frequency and spatial pattern of local mechanical instabilities. As such, the relationship between local architecture and mechanical response should be considered in the design of collagen scaffolds for various applications of tissue engineering.

This study showed that despite being composed of base material with non-linear, soft, and anisotropic mechanical properties, collagen scaffolds have similar stress–strain curves to other porous structures made from stiffer, isotropic, and more brittle materials. Previously identified characteristic stress–strain curves of foams and honeycomb–like structures, composed of materials ranging from aluminum foam to trabecular bone, wood, and elastomeric polymers [15, 27–31], all contain a linear region, plateau region, and densification region [15]. Both collagen scaffolds in this study contained these same three regions. As such, the parameters describing onset of the plateau region and densification region ($\sigma_{Buckling}$, $\sigma_{Densification}$, $\varepsilon_{Buckling}$, and $\varepsilon_{Densification}$) give important information on global compressive behavior of collagen scaffolds. Though collagen scaffolds and other porous structures share the general trend of stress–strain curves, specific global parameters differ depending on the base material. For example, honeycomb panels and foams made from aluminum consistently collapsed at lower compressive strain from 3 to 5% compared to 10% for collagen scaffolds [32–34]. In general, stress was more than an order of magnitude higher in aluminum foams due to the differences in mechanical properties between the two base materials. This data shows how the compressive framework for brittle porous materials provides important insight into the global behavior of collagen scaffolds.

Despite the similarities in global properties and stress–strain behaviors, confocal strain mapping revealed differences in local deformation patterns between the two types of scaffolds. Under compression, honeycomb scaffolds formed visible collapse bands in the middle of each sample. Further deformation was concentrated around these collapse bands, leading to densified regions. In addition, we observed various types of instabilities such as snap-through buckling. In contrast, sponge scaffolds did not form any visible collapse bands, and large deformation was localized near the boundaries. These differences in the deformation pattern led to the distinct local strain distribution between the two types of collagen scaffolds. During the compression, honeycomb scaffolds had relatively unimodal local strain across the construct (Fig. 6), while sponge scaffolds had localized regions of high strains (Figs. 5, 6).

The source of the different local mechanical responses between the two types of collagen scaffolds arises from their geometric characteristics. Cross-sectional images (Fig. 1B) showed honeycomb scaffolds have hexagonal columnar pores. The highly columnar structure leaves the scaffold vulnerable to instabilities. Such instabilities are likely driven by local defects that are randomly distributed throughout

the sample. In fact, confocal imaging demonstrated simultaneous buckling and formation of the global collapse bands around 10% bulk strain (Fig. 4). Similar mechanical responses have been observed in aluminum honeycombs and foams with macro-scale pores (9.53 mm in diameter) [35] and are well predicted by FEA models [16, 36, 37]. The current study used high speed confocal imaging to demonstrate similar phenomenon at the micro-scale.

In contrast to the columnar structure of honeycomb scaffolds, sponge scaffolds had a hierarchical structure with spherical pores of varying sizes embedded in columnar pores (Fig. 1). As a result, sponge scaffolds had many more horizontal reinforcing walls than honeycomb scaffolds. These reinforcements had the effect of reducing the characteristic dimension of the vertical walls and created embedded pores, thus limiting the chances of instability. As such, the mechanical response of the collagen sponge arose from the interplay between the columnar structures and the embedded pores. Under compression, we observed high strain at the boundary of the scaffold, but little evidence of the global collapse bands was detected in the bulk. This strain pattern indicates that the peripheral pores at each boundary failed before the columnar pores could buckle. More specifically, within the peripheral pores, larger pores are more vulnerable to collapse than smaller pores. Hence, larger pores collapsed before other failure modes and dominated the structures' mechanical response. Collectively, these data suggest that the architecture of the peripheral pores contributes greatly to the compressive behavior of the sponge collagen scaffolds.

The mechanical characterization and identification of deformation patterns of collagen scaffolds are crucial for tissue engineering, as the local mechanical environment can affect both the mechanical function of the implants and survivability of the cells embedded in the scaffolds. Current methods for mechanical assessment of collagen scaffolds are mainly focused on the bulk properties such as elastic collapse stress and Young's modulus [15, 38]. Our data suggests that measuring local strain distribution gives complementary information that is necessary to fully capture the mechanical behavior of a collagen scaffold. Both honeycomb and sponge scaffolds had buckling stresses ranging from 2 to 30 kPa and densification stresses from 2 to 37 kPa (Fig. 2B). However, such global parameters do not account for local instabilities, such as snap-through buckling in which the fibers buckle quickly and abruptly. These local instabilities were largely present in the plateau region where global parameters do not characterize in detail. Also, a stark difference in compressive failure modes was observed between scaffold architectures. Honeycomb scaffolds first formed visible collapse bands that propagated throughout the constructs (Fig. 4). Sponge scaffolds did not display a visible collapse band, and all the deformations were concentrated either at the top or bottom edges of the constructs (Fig. 5). These local instabilities may be critical to understanding the probability of local cell death due to loading. Specifically, cell death is expected to occur in larger pores with higher strains first, which could result in reduced new matrix deposition and prolonged periods of localized tissue weakness after implantation. In addition, snap-through instabilities of the pores can induce high local strain rates within the construct. Therefore, optimizing the architecture of collagen scaffolds based on local strain distribution could prevent cell death and ensure the success of a tissue-engineered constructs.

Optimizing the compressive response of collagen scaffolds is a twofold problem where mechanical response and cell biology are closely tied together. Specifically, collagen scaffolds should promote cell proliferation and withstand mechanical load to ensure the survivability of the cells. As previously suggested, both biological factors depend heavily on the distribution of pore sizes within the scaffolds [20, 38]. A variety of scaffold architectures have been used in tissue engineering, including honeycomb-like [39] and sponge-like [40, 41] structures with pore sizes ranging from 80 μm to 325 μm. These architectures were studied and developed based solely on cell attachment, proliferation, and migration. Thus, the relationship between the architecture and local strain distribution within collagen scaffolds is poorly understood. Investigating and understanding these relationships will give insight on designing and optimizing collagen scaffolds to prevent localized compaction zones, as well as fostering cell growth within the scaffolds.

To our knowledge, this is the first study to image and measure the instabilities present within collagen scaffolds used in tissue engineering. We recorded deformation patterns and analyzed the strain distribution using confocal strain mapping technique in combination with Digital Imaging Correlation (DIC). In addition, we detailed local strain maps and identified the relationship between local mechanical behavior of collagen scaffolds. Documenting these instabilities in micro-scale is important as cells living in those scaffolds are in the same scale. Investigating how cells within tissue-engineered constructs behave under strain requires firm understanding of instabilities within collagen scaffolds. In addition, confocal strain mapping technique combined with other microscopy techniques such as Fourier-Tranform Infrared spectroscopy and Raman spectroscopy will give insight on how local composition and mechanical behavior influence the local cell behavior. This combined approach will enable us to investigate the relationship among local composition, strain, and cell death which will give further insight on optimizing architecture for collagen scaffolds. Furthermore, application of modeling techniques that have been used for other porous materials can also be applied to optimize the architecture of collagen scaffolds.

A major challenge of this study comes from comparing the mechanical responses from two distinct experiments, one for exploring global and one for exploring

local response. The global mechanical testing was conducted under a confined compression setting, while local mechanical testing was conducted under an unconfined compression setting. The combination of the two experimental methods is to simulate the *in vivo* condition and to visualize the mechanical response of the material as previously described. The differences in the two experimental techniques created discrepancies in the lateral boundary condition of collagen scaffolds and in the measurement of mechanical properties. In fact, tangent moduli and elastic buckling stresses were significantly lower in the unconfined compression for both types of scaffolds. In addition, densification strains from the confined compression testing were lower because the confined boundary condition enabled collagen scaffolds to densify more easily. However, local instabilities were analyzed far away from the unconfined boundaries and were, therefore, minimally affected by the boundary condition. In addition, during the unconfined compression, some portions within each sample went in and out of the confocal plane, which resulted in the loss of data points during the DIC analysis. However, the missing strain information would account for 8.9% of the total data points. We note that the missing information is in the high local strain region. Therefore, the general trend of the strain distribution would not be affected. Furthermore, the corresponding probability of cell death within the poorly tracked regions exceed the threshold for 100% probability of cell death [14]. Finally, the local strain distribution analysis only considered a two-dimensional confocal plane when the scaffold was three dimensional. This study analyzed one of the two orthogonal planes of symmetry of both types of scaffolds. We believe these scaffolds have some degree of planar isotropy, therefore analyzing one plane of symmetry was sufficient to represent the mechanical responses.

We demonstrated that the global compressive response of collagen scaffolds can be dominated by local instabilities induced during compression. Our data indicated that measuring the global parameters alone is not enough to fully characterize failure patterns of such materials. Under compression, local strain distributions and failure patterns are dependent on the architecture of the collagen scaffolds. Honeycomb-like scaffolds formed collapse bands across the structure, and the deformation propagated from the collapse bands. In contrast, collapse bands in sponge-like scaffolds could not be visually identified, and the deformations were localized near the boundaries. Our findings could be used to design and optimize collagen scaffold architecture to prevent buckling and minimize the probability of cell death within tissue-engineered constructs, leading to a more successful implantation.

Supplementary Information The online version contains supplementary material available at https://doi.org/10.1007/s11340-022-00853-7.

Acknowledgements This study is partially funded by NSF CMMI 2129776 and Histogenics Corp.

Declarations

Conflicts of Interest C.D., S.K., E.B., were full time employees and stockholders of Histogenics Corp. B.K., N.D., J.M., and L.J.B., were partially funded by an award from Histogenics to Cornell University.

References

1. Hunziker EB, Lippuner K, Keel MJB, Shintani N (2015) An educational review of cartilage repair: Precepts & practice - myths & misconceptions - progress & prospects. Osteoarthritis Cartilage 23:334–350. https://doi.org/10.1016/j.joca.2014.12.011
2. Brittberg M (2010) Cell carriers as the next generation of cell therapy for cartilage repair: A review of the matrix-induced autologous chondrocyte implantation procedure. Am J Sports Med 38:1259–1271. https://doi.org/10.1177/0363546509346395
3. O'Brien FJ, Harley BA, Yannas IV, Gibson LJ (2005) The effect of pore size on cell adhesion in collagen-GAG scaffolds. Biomaterials. https://doi.org/10.1016/j.biomaterials.2004.02.052
4. Harley BAC, Gibson LJ (2008) *In vivo* and *in vitro* applications of collagen-GAG scaffolds. Chem Eng J 137:102–121. https://doi.org/10.1016/j.cej.2007.09.009
5. Crawford DC, Heveran CM, Cannon WD et al (2009) An Autologous Cartilage Tissue Implant NeoCart for Treatment of Grade III Chondral Injury to the Distal Femur. Am J Sports Med 37:1334–1343. https://doi.org/10.1177/0363546509333011
6. Kon E, Filardo G, Di Martino A, Marcacci M (2012) ACI and MACI. J Knee Surg 25:17–22. https://doi.org/10.1055/s-0031-1299651
7. Crawford DC, DeBerardino TM, Williams RJ (2012) NeoCart, an autologous cartilage tissue implant, compared with microfracture for treatment of distal femoral cartilage lesions: An FDA phase-II prospective, randomized clinical trial after two years. Journal of Bone and Joint Surgery - Series A 94:979–989. https://doi.org/10.2106/JBJS.K.00533
8. Bingham JT, Papannagari R, Van de velde SK, et al (2008) *In vivo* cartilage contact deformation in the healthy human tibiofemoral joint. Rheumatology 47:1622–1627. https://doi.org/10.1093/rheumatology/ken345
9. Chan DD, Cai L, Butz KD et al (2016) *In vivo* articular cartilage deformation: Noninvasive quantification of intratissue strain during joint contact in the human knee. Sci Rep 6:1–14. https://doi.org/10.1038/srep19220
10. Butz KD, Chan DD, Nauman EA, Neu CP (2011) Stress distributions and material properties determined in articular cartilage from MRI-based finite strains. J Biomech 44:2667–2672. https://doi.org/10.1016/j.jbiomech.2011.08.005
11. Middendorf JM, Diamantides N, Shortkroff S et al (2020) Multiscale Mechanics of Tissue Engineered Cartilage Grown from Human Chondrocytes and Human Induced Pluripotent Stem Cells. J Orthop Res jor 24643. https://doi.org/10.1002/jor.24643
12. Harley BA, Freyman TM, Wong MQ, Gibson LJ (2007) A new technique for calculating individual dermal fibroblast contractile forces generated within collagen-GAG scaffolds. Biophys J 93:2911–2922. https://doi.org/10.1529/biophysj.106.095471
13. Middendorf JM, Shortkroff S, Dugopolski C et al (2017) *In vitro* culture increases mechanical stability of human tissue engineered cartilage constructs by prevention of microscale scaffold buckling. J Biomech 64:77–84. https://doi.org/10.1016/j.jbiomech.2017.09.007

14. Bartell LR, Fortier LA, Bonassar LJ, Cohen I (2015) Measuring microscale strain fields in articular cartilage during rapid impact reveals thresholds for chondrocyte death and a protective role for the superficial layer. J Biomech 48:3440–3446. https://doi.org/10.1016/j.jbiomech.2015.05.035
15. Gibson LJ (2005) Biomechanics of cellular solids. J Biomech 38:377–399. https://doi.org/10.1016/j.jbiomech.2004.09.027
16. Gaitanaros S, Kyriakides S, Kraynik AM (2018) On the crushing of polydisperse foams. European Journal of Mechanics, A/Solids 67:243–253. https://doi.org/10.1016/j.euromechsol.2017.09.010
17. Dong C, Lv Y (2016) Application of collagen scaffold in tissue engineering: Recent advances and new perspectives. Polymers 8:1–20. https://doi.org/10.3390/polym8020042
18. Chan EC, Kuo SM, Kong AM et al (2016) Three dimensional collagen scaffold promotes intrinsic vascularisation for tissue engineering applications. PLoS ONE 11:1–15. https://doi.org/10.1371/journal.pone.0149799
19. George J, Onodera J, Miyata T (2008) Biodegradable honeycomb collagen scaffold for dermal tissue engineering. Journal of Biomedical Materials Research - Part A 87:1103–1111. https://doi.org/10.1002/jbm.a.32277
20. Zhang Q, Lu H, Kawazoe N, Chen G (2014) Pore size effect of collagen scaffolds on cartilage regeneration. Acta Biomater 10:2005–2013. https://doi.org/10.1016/j.actbio.2013.12.042
21. Middendorf JM, Dugopolski C, Kennedy S et al (2020) Heterogeneous matrix deposition in human tissue engineered cartilage changes the local shear modulus and resistance to local construct buckling. J Biomech 105:109760. https://doi.org/10.1016/j.jbiomech.2020.109760
22. Buckley MR, Gleghorn JP, Bonassar LJ, Cohen I (2008) Mapping the depth dependence of shear properties in articular cartilage. J Biomech 41:2430–2437. https://doi.org/10.1016/j.jbiomech.2008.05.021
23. Buckley MR, Bergou AJ, Fouchard J et al (2010) High-resolution spatial mapping of shear properties in cartilage. J Biomech 43:796–800. https://doi.org/10.1016/j.jbiomech.2009.10.012
24. Middendorf JM, Bonassar LJ, Bartell LR, Cohen I (2019) Methods for determining tissue engineered construct readiness
25. Middendorf JM, Griffin DJ, Shortkroff S et al (2017) Mechanical properties and structure-function relationships of human chondrocyte-seeded cartilage constructs after *in vitro* culture. J Orthop Res 35:2298–2306. https://doi.org/10.1002/jor.23535
26. Blaber J, Adair B, Antoniou A (2015) Ncorr: Open-Source 2D Digital Image Correlation Matlab Software. Exp Mech 55:1105–1122. https://doi.org/10.1007/s11340-015-0009-1
27. Crawford R, Jones GF, You L, Wu Q (2011) Compression-dependent permeability measurement for random soft porous media and its implications to lift generation. Chem Eng Sci 66:294–302. https://doi.org/10.1016/j.ces.2010.10.037
28. Lin ASP, Barrows TH, Cartmell SH, Guldberg RE (2003) Microarchitectural and mechanical characterization of oriented porous polymer scaffolds. Biomaterials 24:481–489. https://doi.org/10.1016/S0142-9612(02)00361-7
29. Javid F, Liu J, Shim J et al (2016) Mechanics of instability-induced pattern transformations in elastomeric porous cylinders. J Mech Phys Solids 96:1–17. https://doi.org/10.1016/j.jmps.2016.06.015
30. Salisbury C, Cronin D, Lien F-S (2015) Deformation Mechanics of a Non-Linear Hyper-Viscoelastic Porous Material, Part II: Porous Material Micro-Scale Model. J dynamic behavior mater 1:249–258. https://doi.org/10.1007/s40870-015-0027-1
31. Mercer C, He MY, Wang R, Evans AG (2006) Mechanisms governing the inelastic deformation of cortical bone and application to trabecular bone. Acta Biomater 2:59–68. https://doi.org/10.1016/j.actbio.2005.08.004
32. Kee Paik J, Thayamballi AK, Sung Kim G (1999) Strength characteristics of aluminum honeycomb sandwich panels. Thin-Walled Structures 35:205–231. https://doi.org/10.1016/S0263-8231(99)00026-9
33. Cai L, Zhang D, Zhou S, Xu W (2018) Investigation on Mechanical Properties and Equivalent Model of Aluminum Honeycomb Sandwich Panels. J Mater Eng Perform 27:6585–6596. https://doi.org/10.1007/s11665-018-3771-2
34. Ashab ASM, Ruan D, Lu G et al (2015) Experimental investigation of the mechanical behavior of aluminum honeycombs under quasi-static and dynamic indentation. Mater Des 74:138–149. https://doi.org/10.1016/j.matdes.2015.03.004
35. Wilbert A, Jang WY, Kyriakides S, Floccari JF (2011) Buckling and progressive crushing of laterally loaded honeycomb. Int J Solids Struct 48:803–816. https://doi.org/10.1016/j.ijsolstr.2010.11.014
36. Gaitanaros S, Kyriakides S, Kraynik AM (2012) On the crushing response of random open-cell foams. In: Int J Solids and Struct 2733–2743
37. Jang WY, Kyriakides S (2015) On the buckling and crushing of expanded honeycomb. Int J Mech Sci 91:81–90. https://doi.org/10.1016/j.ijmecsci.2014.02.008
38. Harley BA, Leung JH, Silva ECCM, Gibson LJ (2007) Mechanical characterization of collagen-glycosaminoglycan scaffolds. Acta Biomater 3:463–474. https://doi.org/10.1016/j.actbio.2006.12.009
39. Itoh H, Aso Y, Furuse M et al (2001) A honeycomb collagen carrier for cell culture as a tissue engineering scaffold. Artif Organs 25:213–217. https://doi.org/10.1046/j.1525-1594.2001.025003213.x
40. Freed LE, Vunjak-Novakovic G, Biron RJ et al (1994) Biodegradable Polymer Scaffolds for Tissue Engineering
41. Freyman TM, Yannas IV, Gibson LJ (2001) Cellular materials as porous scaffolds for tissue engineering. Prog Mater Sci 46:273–282. https://doi.org/10.1016/S0079-6425(00)00018-9